


Coexistence of solid and liquid phases in shear jammed colloidal drops

Phalguni Shah ^{1,2}, Srishti Arora^{1,2} & Michelle M. Driscoll ¹✉

Complex fluids exhibit a variety of exotic flow behaviours under high stresses, such as shear thickening and shear jamming. Rheology is a powerful tool to characterise these flow behaviours over the bulk of the fluid. However, this technique is limited in its ability to probe fluid behaviour in a spatially resolved way. Here, we utilise high-speed imaging and the free-surface geometry in drop impact to study the flow of colloidal suspensions. Here, we report observations of coexisting solid and liquid phases due to shear jamming caused by impact. In addition to observing Newtonian-like spreading and bulk shear jamming, we observe the transition between these regimes in the form of localised patches of jammed suspension in the spreading drop. We capture shear jamming as it occurs via a solidification front travelling from the impact point, and show that the speed of this front is set by how far the impact conditions are beyond the shear thickening transition.

¹Department of Physics and Astronomy, Northwestern University, Evanston, IL, US. ²These authors contributed equally: Phalguni Shah, Srishti Arora.
✉email: michelle.driscoll@northwestern.edu

Complex fluids, such as particulate suspensions^{1,2} and polymer solutions³, exhibit a variety of exotic flow behaviours, for instance shear thickening and solidification via jamming. These behaviours are particularly relevant to development of smart materials, such as body armours⁴ and soft robots⁵. Rheometry is traditionally used to characterise complex fluids. However, this technique typically provides measurements averaged over the bulk of the fluid and obscures the information on local variations in flow. The free-surface geometry in drop impact systems offers a unique lens to probe these flow properties, as it provides data on manifestations of non-Newtonian flow with high spatial and temporal resolution.

An extensive understanding has been developed for the dynamics of a Newtonian fluid drop impacting a dry solid substrate^{6–11}. However, the vastly different flow properties of complex fluids substantially modify impact dynamics. Past studies have explored the spreading and splashing of a variety of polymeric fluids^{12,13} and particulate suspensions^{14–19}; however each has largely focused on a relatively narrow slice of the vast parameter space. The role of particulate additives in controlling the splashing transition has been explored^{14,15}, as well as the spreading and jamming of dense suspension drops^{16–19}. In particular, experiments on impacting shear thickening fluids have reported solid-like states after impact^{16–18}. Colloidal suspensions offer a convenient control parameter — volume fraction — to scan suspension behaviours ranging from Newtonian-like to shear thickening.

Shear thickening — an increase in viscosity with increasing shear — is one of the most counterintuitive phenomena exhibited by dense suspensions^{1,2}. The Peclet number, $Pe = \frac{\text{shear rate}}{\text{rate of diffusion}}$, is a dimensionless number used to quantify high shear rates, and we expect the onset of shear thickening at $Pe \gg 1$. The transition to shear thickening occurs when a suspension with relatively high ϕ is subjected to a shear higher than a critical value^{1,20–22}. We note that for our experimental parameters, $Pe > 10^2$, and thus we expect shear thickening after impact in the high- ϕ limit. Many rheological studies have focused on elucidating the mechanism of shear thickening, and both lubrication hydrodynamics and particle interactions have been shown to play a role. Shear thickening has been proposed as precursor to shear jamming, and the nature of this transition is an active field of study. For a more detailed discussion, we refer the reader to the following reviews^{2,20–22}.

Here, we use high-speed imaging to study the drop impact of colloidal suspensions over a large range of volume fractions ($0.09 \leq \phi \leq 0.50$) and impact velocities ($0.7 \text{ m/s} \leq u_0 \leq 4.0 \text{ m/s}$), thus sampling impact behaviour from liquid-like spreading to solid-like shear jamming. Our highly time-resolved data allows us to characterize the transition to shear jamming in detail, and provides valuable insights about the effects of high instantaneous shear on fluid properties. Combined with input from rheological data, our measurements offer a more holistic picture of complex fluid flow, especially under dynamic conditions. The results we present here take us closer to an understanding of the shear jamming transition and the properties of shear jammed solids.

Results

For our experiments, we synthesize charge-stabilized silica spheres (diameter $2a = 830 \pm 20 \text{ nm}$, Fig. 1a) using the Stöber process^{23,24} and suspend them in water. The sedimentation time is the time a sphere takes to sediment freely over its radius a ²⁵, calculated as:

$$t_s = \frac{9\eta}{2\Delta\rho ga}, \quad (1)$$

where η is the dynamic viscosity of the suspending fluid (water in this case), $\Delta\rho$ is the density difference ($\rho_{\text{silica}} - \rho_{\text{water}} = 1 \text{ g/cm}^3$),

$g = 9.8 \text{ m/s}^2$, and $a = 415 \text{ nm}$, the radius of the particle. Calculated in this manner, $t_s = 1.1 \text{ s}$. Therefore, the characteristic time for a particle to sediment over the lengthscale of the drop ($d_0 = 3 \text{ mm}$) is $t_s^{\text{drop}} = 4000 \text{ seconds}$, or over an hour. Thus, the time for our silica sphere to sediment over the size of the droplet is much longer than the time of the experiment. This calculation for dilute suspensions has been shown to be modified by a factor smaller than 1, up to $\phi = 0.30$ ²⁶. Therefore, for our system, this calculation serves as an upper-bound estimate. To further decrease sedimentation effects, all samples are re-suspended immediately before every trial using a vortex mixer. Spherical drops of diameter $d_0 = 3.0 \pm 0.1 \text{ mm}$ are formed by drawing a known volume of fluid ($15 \mu\text{L}$) into a micropipette. We set the impact velocity by changing the height from which the drops are released, and record the drops impacting on a dry, hydrophilic glass substrate using a high-speed camera. We note that the contact angle of gently deposited suspensions on the glass substrate is practically constant with increasing ϕ , around 4° (for more details, see Supplementary Note 1). All experiments are performed in a humidity chamber, which additionally mitigates air currents (see Methods for details). Data is analysed via ImageJ, and plotted using python. Error bars reported are one standard deviation over at least 5 trials (one standard deviation corresponds to a 68% confidence interval).

To connect impact behaviours with rheological properties, a mapping between impact velocity and rheological parameters such as shear rate or shear stress is necessary. Precisely quantifying shear rates in drop impact systems is challenging due to the nonuniformity of shear in both space and time. However, a simple dimensional argument can be used to estimate the shear rate at impact. At the instant of impact, the bottom point of the drop comes to rest, while the apex continues to fall at the impact velocity u_0 , as the shear caused by impact has not had time to propagate across the drop. Dividing this difference in speeds, u_0 , by the drop size d_0 thus provides an estimate of the maximum shear rate at the moment of impact: $\dot{\gamma}_{\text{impact}} = u_0/d_0$. With the drop size of 3 mm, we could access shear rates in the range $233 \text{ s}^{-1} \leq \dot{\gamma}_{\text{impact}} \leq 1333 \text{ s}^{-1}$. Thus, we are able to span a large spectrum of flow behaviours in these suspensions, and observe how non-Newtonian flow gives rise to a rich variety of impact phenomena.

Bulk rheometry measurements [Fig. 1b] demonstrate the variety of flow behaviours exhibited by our suspensions. At low ϕ (black and pink lines), the fluid viscosity is constant, akin to a Newtonian fluid. Shear thinning (decreasing viscosity) becomes pronounced as ϕ is increased (green and purple curves), and shear thickening (indicated by increasing viscosity) appears for $\phi \geq 0.47$ at high shear stresses (shear stress above 100 Pa, orange, blue, and red curves). We observe fascinating consequences of this non-Newtonian rheology in our impact experiments. At $\phi = 0.47$, where weak shear thickening appears at high stresses in bulk rheology, we observe patches of localised solidification during spreading — panel 3 of Fig. 2a shows small solid-like bumps that protrude from the spreading drop, but vanish in panels 4 and 5 [Video S11²⁷]. At higher ϕ , we observe partial solidification of the drop — Panel 2 in Fig. 2b shows that the bottom part of the drop acts as a solid, while the top part remains fluid and flows over the solidified region throughout panels 3–5 [Video S12²⁷]. Finally, at $\phi = 0.49$ and high impact velocities, most of drop solidifies as shown in Fig. 2c [Video S13²⁷]. Here, we show that this variety of solidification behaviours is a direct consequence of shear jamming²⁸, evidenced by their occurrence much below the static jamming threshold²⁹.

We encapsulate this broad range of impact outcomes in a $\phi - u_0$ state diagram [Fig. 3]. Green circles, indicating simple spreading [Video S14²⁷], dominate the low ϕ and low u_0 region. With increasing ϕ or u_0 , the localised solidification regime

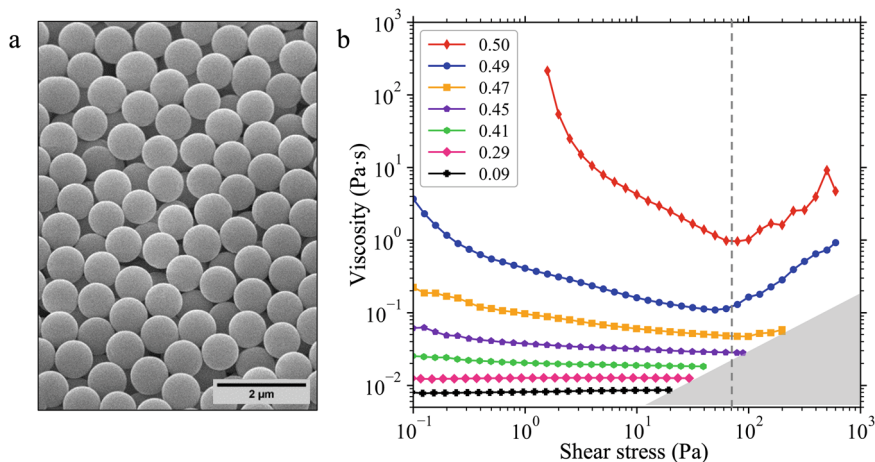


Fig. 1 Rheology of the colloidal suspensions. **a** SEM image of the colloidal silica spheres used in our drop impact experiments; the sphere diameter is 830 ± 20 nm. **b** Bulk rheological flow curves: the colloidal suspension exhibits viscous flow, shear thinning, and shear thickening as ϕ is increased. The grey triangle in the bottom right indicates the rate limit of the rheometer.

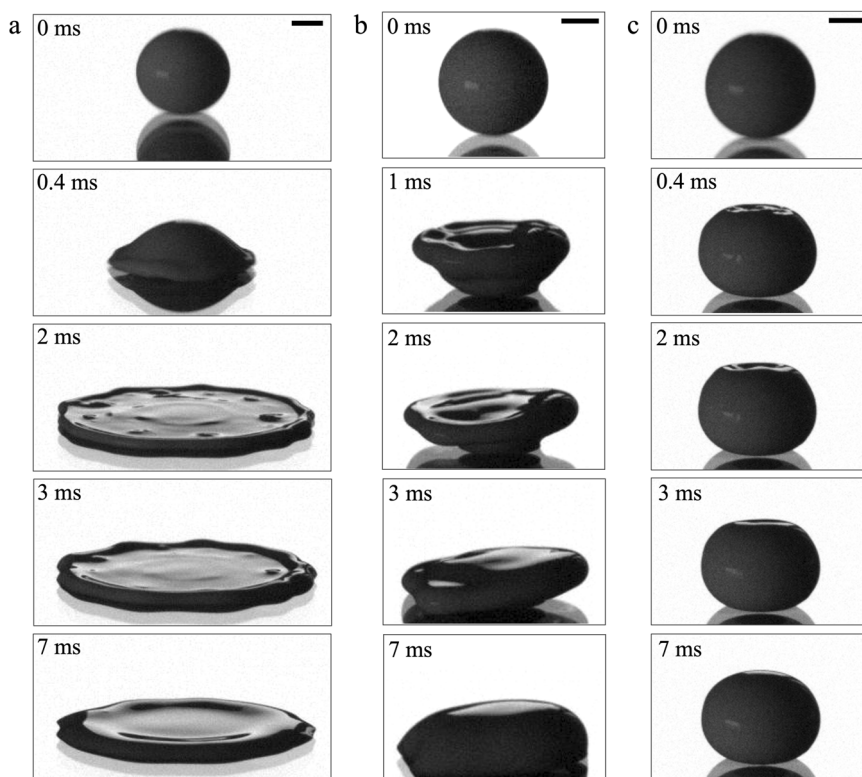


Fig. 2 Exotic impact behaviours of colloidal suspension drops. **a** Timeseries of a $\phi = 0.47$ colloidal drop expanding after impacting at $u_0 = 3.0$ m/s [Video SI1²⁷]. The spreading drop shows transient pockets of localized solidification, indicating the onset of shear thickening. **b** Timeseries of a $\phi = 0.49$ colloidal drop impacting at $u_0 = 2.0$ m/s [see also Video SI2]. The bottom half of the drop solidifies, while the still-fluid top portion flows over it. **c** Timeseries of a $\phi = 0.49$ drop impacting at $u_0 = 3.0$ m/s [Video SI3²⁷]. While most of the drop is solidified, the top portion of the drop is in the liquid phase. All scale bars are 1 mm.

appears (orange diamonds), followed by the bulk solidification regime (blue triangles), where a larger and larger portion of the drop solidifies upon impact. The transition between these regimes is a function of both ϕ and u_0 , as all regimes can be accessed by varying either of the parameters while keeping the other constant. Additionally, we find that the drop behaviour is very sensitive to small changes in ϕ , consistent with the transition to shear thickening in rheological measurements [Fig. 1b].

To quantify this range of impact outcomes, we compute the normalized maximum diameter of the impacted drops,

$\beta = d_{max}/d_0$, and plot this metric against u_0 [Fig. 4a]. For $\phi \leq 0.47$, β increases with increasing impact velocity. However, β drops to 1 at $\phi \geq 0.49$ and high impact velocities. This is because the drop no longer spreads after impact (lower inset). This result is consistent with recent studies that observed similar solidification in suspension impact at high ϕ ^{16,18}. Our drops remain solid for a few milliseconds; however, they spread like a liquid over the timescale of a second [Video SI5²⁷]. Thus, the solid-like state we observe is transient in nature, further evidence that this solidification is a direct result of shear jamming. A recent result suggests that the

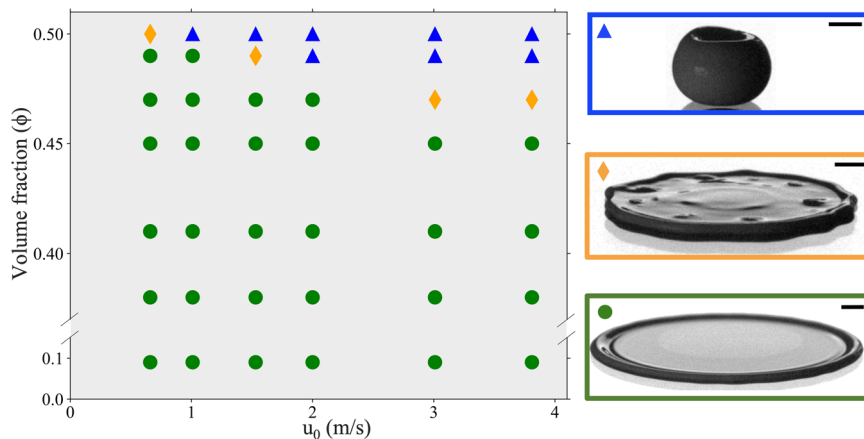


Fig. 3 State diagram of colloidal drop impact. $\phi - u_0$ state diagram summarizing impact regimes; representative snapshots corresponding to these regimes are shown on the right. Green circles denote simple spreading behaviour, which dominates the low ϕ , low u_0 region. Orange diamonds indicate that transient pockets of localised solidification were observed during spreading. Blue triangles correspond to the partial/full solidification regime, where the bottom portion of the drop jams after impact, but a shrinking region at the top remains fluid. Scale bars are 1 mm.

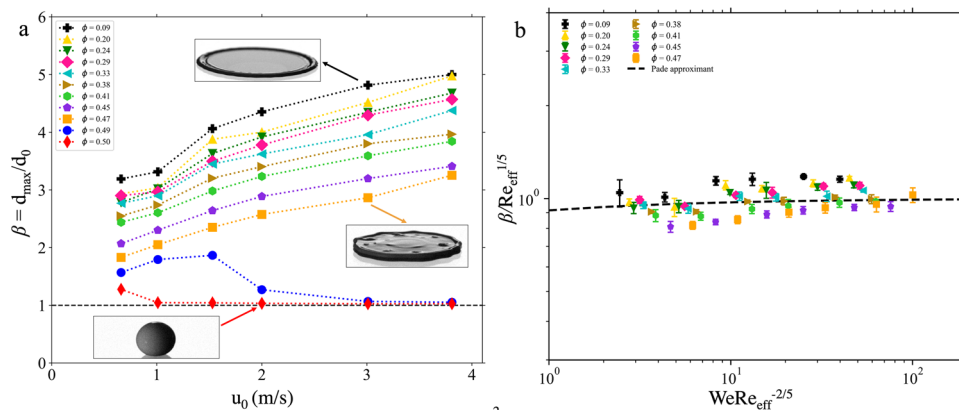


Fig. 4 Quantifying maximum drop spreading. **a** Normalised maximum diameter, $\beta = d_{max}/d_0$, as a function of u_0 for various volume fractions ϕ . For $\phi \geq 0.49$ and high impact velocities, β drops to 1, indicating the drop does not spread. Insets show representative snapshots of simple spreading (upper), localised solidification (middle), and bulk solidification (lower). Dotted lines are guides to the eye, and the dashed black line indicates $\beta = 1$. **b** $\beta/Re_{eff}^{1/5}$ for $\phi \leq 0.47$, plotted against the dimensionless parameter $WeRe_{eff}^{-2/5}$. The dashed black line is the first-order Padé approximant as reported by Laan et al.⁸ [Eq. (3)] for Newtonian fluids, fit to our data. Considering the strongly shear-thinning nature of our suspensions, the data shows a good agreement with the Newtonian model.

substrate wettability affects this timescale of unjamming¹⁸, but this problem remains largely unexplored.

At $\phi \leq 0.47$, the drops spread in a manner qualitatively similar to Newtonian fluids [Video S14²⁷]. Previous experiments⁸ with Newtonian fluids have shown that $\beta/Re_{eff}^{1/5}$ scales as the dimensionless parameter $WeRe_{eff}^{-2/5}$, where We is the impact Weber number, $\rho u_0^2 d_0 / \sigma$, and Re is the Reynolds number, $Re = \rho u_0 d_0 / \eta$. Here, σ is the surface tension of the suspending fluid (for this case water, $\sigma = 72$ mN/m), ρ is the fluid density, calculated as:

$$\rho = \rho_{silica}\phi + \rho_{water}(1 - \phi) \tag{2}$$

with $\rho_{silica} = 2000$ kg/m³ and $\rho_{water} = 1000$ kg/m³, and η is the suspension viscosity. For impacting colloidal drops, the calculation for the Weber number remains identical to Newtonian fluids. Estimating the Reynolds number, however, is less straightforward due to the non-constant fluid viscosity of complex fluids. During the spreading phase, the maximum shear rate can be estimated as $\dot{\gamma}_{spr} \sim u_0/l$, where l is the minimal thickness of the expanding fluid layer. Past work has established that $l \sim 100$ μ m for the range of fluid parameters relevant to this work⁶. Estimated this way, the $\dot{\gamma}_{spr}$ values we obtain are of the order 10^4 s⁻¹. Measurements of

fluid viscosity at such high shear rates cannot be made via conventional rheometry. Therefore, we use the fluid viscosity at the highest accessible shear rate from our rheology data (see Supplementary Note 2). For our experimental conditions, the range of dimensionless numbers was $20 < We < 1000$ and $50 < Re_{eff} < 1600$. In Fig. 4b, we plot $\beta/Re_{eff}^{1/5}$ against $WeRe_{eff}^{-2/5}$ in the spreading regime. The dashed black line is the first-order Padé approximant fit to our data:

$$\frac{\beta}{Re_{eff}^{1/5}} = \frac{(WeRe_{eff}^{-2/5})^{1/2}}{A + (WeRe_{eff}^{-2/5})^{1/2}}. \tag{3}$$

This equation was reported by Laan et al.⁸ to interpolate between the inertial and viscous regimes. The parameters $Re_{eff}^{1/5}$ and $WeRe_{eff}^{-2/5}$ are based on scaling arguments that consider the balance of inertial, viscous, and capillary effects^{6,8}. For our data, the fit returns $A = 0.09 \pm 0.01$, much smaller than $A = 1.24 \pm 0.01$ reported for Newtonian fluids⁸. Nevertheless, given that the fluids considered in this study are highly shear thinning at higher ϕ , the agreement we report here with Newtonian models is surprising. Our data also shows good agreement with an empirical fit reported

by Scheller et al.³⁰. Recent work has additionally reported a scaling correcting for surface wettability⁹; see Supplementary Note 3 for a further discussion of these models.

In the localised solidification regime [orange diamonds in Fig. 3, Video S11²⁷] the bulk of the drop still spreads like a Newtonian fluid [Fig. 4b], but shear thickening is apparent via solidified patches that appear and then disappear. These patches appear during the spreading phase, around 1 millisecond after impact. However, indicators of jamming are present earlier, in the form of nonuniformity in the spreading rim of the drop [see for example, panel 2 in Fig. 2a]. In most cases, these patches outlive the spreading phase and disappear during the receding phase, over tens of milliseconds. Our observation of this regime coincides with the onset of weak shear thickening in the bulk rheology data [orange curve in Fig. 1b]. Moreover, the transient nature of these patches is strong evidence that regions of high viscosity are embedded in a lower-viscosity fluid phase. We note that we can only observe these patches on the drop surface in high-speed imaging data, and there is a large variance in the spatial and temporal distribution of these patches. This limits our ability to extract quantitative information about localised jamming. For higher ϕ , where shear thickening is pronounced, the drop exhibits drastically different behaviour, and does not spread at all.

For $\phi \geq 0.49$, a large fraction of the drop solidifies upon impact. To quantify the dynamics of this partially solidified state, we measure the height of the drop apex as a function of time [Fig. 5a]. Consistent with another study of impacting shear-thickening drops¹⁶, we observe two regimes in the h vs. t curve — a free-fall regime and a plateau regime. Immediately after impact, h decreases at a rate identical to the impact velocity (free-fall regime) [Fig. 5b], and then plateaus at a constant value, h_{min} (plateau regime). This is strong evidence that any shear from the impact event has not yet propagated to the top portion of the drop, and hence the top portion must still remain a liquid. Studies of impacting Newtonian drops have also observed a similar ‘free-fall’ regime where the drop apex moves at the impact velocity^{10,31,32}. It is worth noting that in contrast to Newtonian fluids, where a broad transition regime was observed between the free-fall and the plateau regimes, we observe a sudden transition from the free-fall to plateau regime [Fig. 5a], a direct indication of a shear jammed drop.

We quantify the spatial extent of solidification by plotting the normalized minimum height, h_{min}/d_0 against u_0 [Fig. 5c]. The increase in h_{min}/d_0 with u_0 indicates that a larger and larger

volume of the drop is solidified as the impact velocity is increased. Interestingly, at high impact velocities, h_{min}/d_0 plateaus to a value smaller than 1, indicating that the solidified drop also undergoes deformation along the impact direction, along with slight bulging in the plane transverse to impact [Fig. 2c]. Furthermore, the high temporal resolution (100,000 fps) of our imaging enables us to capture the details of this solidification as it occurs.

Immediately after impact, we observe a disturbance travelling upward along the drop surface over hundreds of microseconds [orange and green arrows in Fig. 6a].

To better visualise this front, we subtract successive frames of the image sequence, so that only the parts that change between frames are highlighted [right panel of Fig. 6a, Video S16²⁷]. The location of the front is given by the lower end of the bright edge [Fig. 6b]. As this front travels upward, the portion of the drop above the front still maintains its pre-impact curvature [red circles in Fig. 6a], indicating that it is unaffected by the impact event until the front reaches it (consistent with $u^* = u_0$, Fig. 5b). The angular location of this front plotted against time reveals that the front travels at a constant speed, u_{front} [slope of the line in Fig. 6c]. u_{front} increases with increasing u_0 , and its value is several times larger than u_0 [Fig. 6d]. As evident from the rheology, the suspension thickens when the applied shear surpasses a critical value. Indicated by the dotted lines in Fig. 6e, the critical shear rate where thickening is observed, $\dot{\gamma}_c$, is much lower for $\phi = 0.50$ than for $\phi = 0.49$. We plot u_{front} against the excess shear rate over this critical value, $\dot{\gamma}_{impact} - \dot{\gamma}_c$, and the data indeed collapses on a single curve for both ϕ [Fig. 6f]. This suggests that the speed of this disturbance is set by this excess shear rate; the physical relevance of this excess shear rate is discussed in the following section.

As the impact velocity is increased, a larger and larger volume of the drop solidifies upon impact. At $\phi = 0.50$ and $u_0 = 4$ m/s, we observe that the drop bounces off the substrate, with the coefficient of restitution $\epsilon = 0.1$ [Video S17²⁷]. This rebound behaviour is especially striking given the hydrophilic nature of the substrate. By coupling this coefficient of restitution with the drop’s deformation along the impact axis, we can semi-empirically estimate the elastic modulus of the solidified drop. The drop impacts the substrate with an initial velocity u_0 , remains in contact with the substrate for time $\Delta t = 200 \mu$ s, and then rebounds with the final velocity ϵu_0 . While in contact with the substrate, we measure that the drop is deformed in the direction of impact by the amount $\Delta x = 0.24$ mm. We calculate the force experienced by the drop

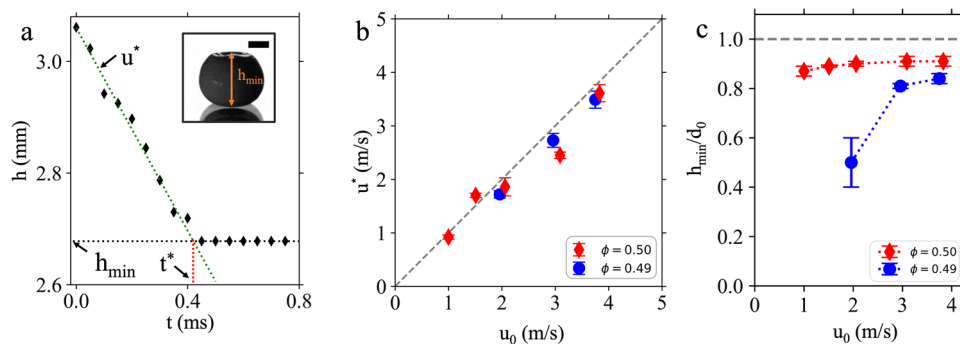


Fig. 5 Characterisation of the partial solidification regime. **a** Height of the drop apex from the impact substrate, plotted against time, for $\phi = 0.50$, $u_0 = 3$ m/s. h decreases at the speed u^* until time t^* , then plateaus at the value h_{min} . Inset: post-impact snapshot of a drop at the minimum height h_{min} . Scale bar in the inset is 1 mm. **b** h decreases at a speed identical to the impact velocity, indicating that over the timescale t^* , the top portion of the drop is unaffected by the impact event. u^* is computed as the slope of the linear fit to the decreasing part of h vs. t data, error bars indicating the standard deviation over at least 5 trials. Dashed line corresponds to $u^* = u_0$. **c** h_{min}/d_0 vs. impact velocity u_0 . h_{min}/d_0 increases with increasing impact velocity, and then plateaus at a value less than 1, indicating finite compression of the drop along impact axis. Dashed line indicates $h_{min}/d_0 = 1$. Error bars indicate one standard deviation over at least 5 trials.

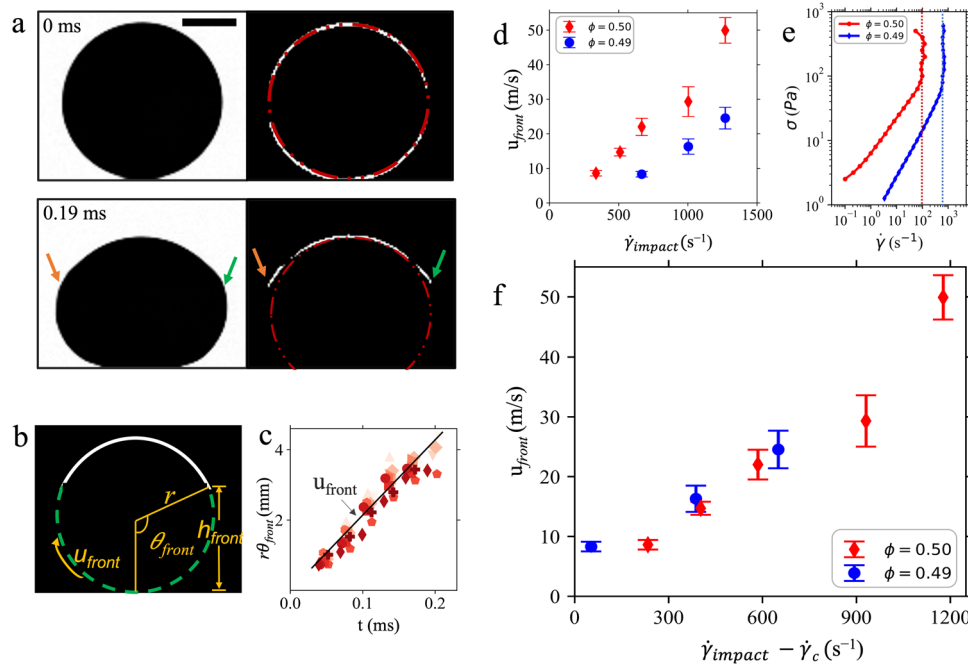


Fig. 6 Dynamics of the solidification front. **a** Timeseries of a $\phi = 0.50$ drop impacting at $u_0 = 2.0$ m/s [Video S16²⁷]. Right panels are images obtained by subtracting consecutive frames, so that the edge of the solidification front is highlighted (shown by arrows). The red circle indicates the drop profile before impact. Even at 0.19 ms, the portion of the drop above the front maintains its pre-impact curvature. Scale bar is 1 mm. **b** Schematic of a subtracted image of the moving solidification front, outlining relevant parameters. The height, h_{front} , of the edge of the white outline gives the location of the front, which is then converted to $r\theta_{front}$ using the spherical geometry. **c** Example datasets of $r\theta_{front}$ vs. t for $\phi = 0.49$ and $u_0 = 3$ m/s. $r\theta$ vs. t is a straight line, the slope being the front speed along the surface, u_{front} . **d** u_{front} plotted against $\dot{\gamma}_{impact}$. **e** High- ϕ bulk rheological data from Fig. 1b re-plotted as shear stress vs. shear rate. Dotted lines indicate the onset shear rates $\dot{\gamma}_c$ for shear thickening. **f** The u_{front} data for $\phi = 0.49$ and $\phi = 0.50$, when plotted against $\dot{\gamma}_{impact} - \dot{\gamma}_c$, collapses on a single curve. In all panels, error bars indicate one standard deviation over at least 5 trials.

upon impact using momentum conservation:

$$F = \frac{m\Delta u}{\Delta t} = \frac{m(1 + \epsilon)u_0}{\Delta t}, \quad (4)$$

To convert the force to a stress, we divide by the contact area for a Hertzian contact³³, $\pi a^2 = \pi d_0 \Delta x / 2$:

$$\sigma = \frac{F}{\pi d_0 \Delta x / 2} = \frac{2m(1 + \epsilon)u_0}{\pi d_0 \Delta x \Delta t}. \quad (5)$$

The strain experienced by the drop is $\gamma = \Delta x / d_0$. Thus, the elastic modulus of the rebounding drop can be computed as

$$E = \frac{\sigma}{\gamma} = \frac{2m(1 + \epsilon)u_0}{\pi(\Delta x)^2 \Delta t}. \quad (6)$$

using $m = 2.25 \times 10^{-5}$ kg, we find $E = 5$ MPa. A more thorough estimate using Hertz's equations³³ for two colliding elastic bodies leads to a similar estimate of E . Calculating the elastic modulus in this way for other impact conditions is challenging, as measuring the contact time in the absence of rebound is nontrivial.

Discussion

In sum, our analysis presents the following picture of the drop dynamics. Upon impact, the drop experiences a large instantaneous shear at the impact point. At high enough volume fractions and impact velocities, this stress manifests itself as pockets of localised solidification embedded in the spreading liquid phase. At even higher volume fractions or shear, a larger and larger fraction of the drop solidifies after impact, but some volume at the top remains liquid. Therefore, the shear front must be dissipating as it moves upward, and the stress falls below the critical stress for shear thickening before the entirety of the drop is solidified. Moreover, at the highest impact velocity, the drop

rebounds, and the coefficient of restitution allows us to estimate the elastic modulus of the shear jammed solid, $E = 5$ MPa. Thus, our drop impact experiments provide a unique window to observe shear jamming as it occurs, and give rise to a number of questions about the nature of both the shear jamming transition and the resulting jammed solid.

The occurrence of localised solidification coincides with the appearance of weak shear thickening in our bulk rheology data. The fact that these solidified patches vanish over tens of milliseconds is strong evidence that they are regions of high viscosity embedded in a lower-viscosity fluid phase. Recent rheological studies using boundary stress measurements (BSM) have reported finite regions of enhanced stress in silica suspensions^{34–36}. In these works, Rathee et al.^{34–36} argued that the transition from shear thickening to shear jamming is governed by the growing size of such localised shear jammed regions. Our observations of transient localized solidification are thus striking visual evidence of such a mechanism. Further spatially resolved stress measurements performed on impacting drops¹¹ could provide more information on the nature of localised solidification in free-surface systems.

In the bulk solidification regime, the coexistence of liquid and solid regions is a result of shear traveling upward from the impact point, and simultaneously dissipating due to the high suspension viscosity. Although recent studies of Newtonian fluids for a large range of viscosities^{7,10} have established the velocity and pressure fields within an impacting drop, they are not directly applicable in case of colloidal systems due to their highly non-Newtonian nature. Numerical work investigating transient shear might be a useful next step to uncover the mechanism of dissipating shear fronts. Though challenging, measurements of the flow inside the drop via methods such as

particle tracking would provide key information about the flow field in an impacting colloidal drop.

The nature of the upward-travelling front raises a number of interesting questions. Before the front reaches the top, the speed of the drop apex u^* is identical to u_0 [Fig. 5b], and the curvature of the top portion is the same as it was before impact. This confirms that the information of the impact event reaches the top portion only with the front, thus establishing that it is a solidification front. Why the speed of this front is constant along the drop surface is an intriguing question. One would expect a shear front to travel through the bulk of the drop, upward from the region in contact with the substrate. Given the visual nature of our measurements on an opaque drop, we can naturally observe this front only on the surface. The most likely explanation, therefore, is that the front we measure is this bulk shear front after it interacts with the drop boundary.

Our experiments are especially well-positioned to capture such a front due to the free-surface conditions here that are absent in other studies of shear fronts. Past work has established that shear fronts in dense suspensions are not a result of densification³⁷, and their velocity is set by the external driving speed^{37–41}. We are able to characterise the dependence of the front speed on applied shear rate due to the unique capability of the drop impact system to apply large and instantaneous shear. At a first glance, Fig. 6e suggests that reaching a shear rate beyond the critical value is impossible, making an excess rate beyond the critical value unphysical. However, we argue here that this is meaningful for drop impact systems. In a rheometer, resistance to shear in a thickened fluid causes the shear rate to not increase even though applied shear stress increases [Fig. 6e]. However, at the instant of impact, the shear rate estimated by $\dot{\gamma} = u_0/d_0$ is a physically relevant quantity. The rationale is as follows: at the moment of impact (before the front has travelled across the drop over ~ 100 microseconds, Fig. 6a, b), the impact point comes to an abrupt halt while the drop apex still moves at the impact velocity [Fig. 5b]. Therefore, the velocity difference of u_0 exists across the drop size d_0 , leading to $\dot{\gamma} = u_0/d_0$. The front propagation gives us a timescale over which effects of shear jamming are apparent over the whole drop, and we believe that the inability to access high shear rates in a rheometer is a direct consequence of the longer timescale (typically a few seconds) over which shear is applied in rheometry measurements. We emphasize this ability to apply instantaneous high shear is the greatest strength of studying suspension behaviour via drop impact.

The dependence of the front speed on $\dot{\gamma}_{\text{impact}} - \dot{\gamma}_c$ in our experiments [Fig. 6f] suggests that the suspension properties near the shear jamming transition are governed by the distance from the onset of shear thickening. This is consistent with measurements in static jamming, where material properties depend on the distance from the critical point⁴². The functional form of this dependence potentially contains insights into the nature of the shear jamming transition. Numerical work exploring the impact of suspension drops, although incredibly challenging due to the strong role of hydrodynamics in colloidal systems, might provide crucial information in this respect. Unfolding the physics of these fronts will not only extend constitutive models for complex fluid rheology to much higher stress regimes, but will also help us understand more about the nature of the shear jamming transition.

Due to the transient nature of the shear jammed state, characterising the jammed solid created after impact is challenging. Using the coefficient of restitution of the rebounding drop, we were able to estimate the elastic modulus of the solid phase, $E = 5$ MPa. As rebound only occurred at one impact velocity, how the elastic properties of shear jammed drops are controlled by the impact conditions remains obscure. The use of superhydrophobic

substrates promotes rebound, even in Newtonian liquid drops⁴³. Further colloidal drop impact experiments on superhydrophobic surfaces could extend the parameter space where drops rebound, and thus provide the information essential to understand what controls the properties of this elastic state. Numerous other properties of the shear jammed solid are of interest: When and how would such a solid fracture? How broad is its linear elastic regime? How do these properties compare to those of static jammed solids?

In conclusion, we conduct highly time-resolved drop impact experiments and systematically probe suspension flow ranging from Newtonian-like to shear jamming. We show that the impact behaviour in the spreading regime can be quantitatively understood via an effective viscosity framework, and that the solidification behaviours at high ϕ and u_0 are direct consequences of shear jamming. The free-surface geometry in our system provides direct visual information on how the shear jamming transition occurs, both in parameter space and in time. Shear jamming occurs via a solidification front, the speed of which is set by how far into the shear thickening regime the applied shear rate is. Furthermore, we see this transition occur via a localised solidification regime that cannot be observed via bulk measurements. We believe that drop impact is a powerful experimental tool to investigate macroscopic properties of complex fluids, and provides information that compliments the data from bulk rheometry.

Methods

Colloidal sample preparation. We fabricated silica spheres in our lab using the Stöber^{23,24} synthesis method. The particle size was determined by the number of feeds: we performed 14 feeds after the initiation of the reaction, resulting in particles with a diameter of 830 ± 20 nm. The reaction mixture was centrifuged and re-suspended in ethanol 3 times; the suspension was then gravity separated to improve monodispersity. The particles were then imaged on the Hitachi S4800 Scanning Electron Microscope [Fig. 1a]. The particle size was characterized by measuring the diameter of a representative sample of 100 particles in ImageJ, and the polydispersity reported is the standard deviation in particle size.

A concentrated stock suspension of the silica spheres was prepared in water (with no surfactant), and the weight fraction was measured by drying $100 \mu\text{L}$ of the stock suspension. The density of silica (2 g/cm^3) was used to convert weight fractions into volume fractions. Dilutions were then performed to prepare samples of desired volume fractions. The uncertainty in volume fractions reported is 0.5% (0.005) or less, determined by repeated measurements. When not in use, all the sample tubes were sealed using Parafilm and stored in a refrigerator to minimize evaporation and contamination.

Experimental setup. We used Fisherbrand plain glass slides as the hydrophilic impact substrate. The slides were cleaned using a 2.5 M solution of NaOH in ethanol and water to remove organic impurities. A micropipette was used to form colloidal drops. The micropipette was mounted on a vertically moving pipette holder to vary impact velocities. We used $15 \mu\text{L}$ of fluid to obtain drops of $3.0 \pm 0.1 \text{ mm}$ diameter. The setup was enclosed in a humidity chamber with the relative humidity maintained between 70–80% using a saturated solution of NaCl in water, and the humidity was monitored in real time during experiments. Before every trial of the impact experiments, a vortex mixer was used to re-disperse the sample, ensuring that it was consistently well-mixed. The experiment was repeated at least 5 times for each impact condition to ensure reproducibility.

The impacting drops were backlit using a white LED light, and filmed using two high-speed cameras. The first camera, a Phantom V2512, captured the side-view of the impacting drop at 100,000 frames per second. The second camera, a Phantom V640L, filmed at 20,000 fps. It was tilted at an angle of 15° to gather information on how the impact affected the top surface of the drop. The spatial resolution of the data collected from both cameras was so that the size of a single pixel is approximately $40 \mu\text{m} \times 40 \mu\text{m}$.

Rheological studies. Stress-controlled rheological measurements were performed on the colloidal samples over $0.09 \leq \phi \leq 0.50$. The measurements were done on a TA Instruments Discovery HR-2 rheometer at room temperature ($\sim 21^\circ\text{C}$) using the cone-plate geometry with 40 mm diameter and a 1° cone angle. The truncation gap was $25 \mu\text{m}$. We covered the edges of the samples with a microscope immersion oil to minimize evaporation. The samples were pre-sheared to remove effects of shear history.

Data analysis. All high-speed videos were background-divided and analysed using ImageJ. The plots were made using python, and all errors reported are one standard deviation calculated over at least 5 trials (corresponding to a 68% confidence interval). To experimentally verify the impact velocities, the drop position in the high-speed videos was measured over the distance of at least 10 mm before impact. The impact velocity, u_0 , was obtained as the slope of the least squares linear fit of the position-time data. The maximum drop spread d_{max} was determined by locating the frame in the impact timeseries where the extent of the spreading drop was the greatest.

The height of the tallest point on the drop relative to the substrate, h , was measured for each frame in the image sequence. The speed of the drop apex after impact, u^* , was computed as the slope of the least-square fit to the h vs. t data in the free-fall regime. The minimum height, h_{min} , was defined as the drop height at the crossover point between the free-fall and plateau regimes in the h vs. t plot. The time of first observation of h_{min} measured since the impact event, was defined as t^* . The slope of the linearly decreasing regime in the h vs. t plot was defined as u^* . To calculate the coefficient of restitution, the speed of the drop before impact u_0 , and the speed after rebound, u_f were computed using several frames of the image sequence. The coefficient of restitution was then computed as $\epsilon = u_f/u_0$.

To calculate the speed of the upward-moving front, the side-view impact videos recorded at 100,000 fps were used. For every frame of the image sequence, the pixel-wise difference between consecutive frames was taken in ImageJ, so that only the elements that changed between consecutive frames (corresponding to the location of the moving front) were highlighted [Video SI727]. This enabled us to locate the jamming front with a time uncertainty of 10 μ s. The images were then adjusted for brightness and contrast to enhance the moving front. The vertical height h_{front} of the disturbance from the impact substrate was measured for each frame of the image sequence, until the front was no longer visible. For every high-speed video, the left and right half of the drop were separately analyzed to obtain two datasets for $h_{front}(t)$. In order to convert h_{front} to the position along the drop surface, $r\theta_{front}(t)$, we approximated the drop profile as a circle of radius $r = 1.5$ mm (disregarding the slight deviation from spherical shape during front propagation), and used the relation $h_{front}(t) = r(1 - \cos\theta_{front}(t))$, such that $\theta_{front}(0) = 0$ at the impact point, to obtain the angle $\theta_{front}(t)$. A line was then fit to the $r\theta_{front}$ vs. time plots, and the slope, averaged over the two halves of the drop and several movies for each impact condition [Fig. 6c], was reported as u_{front} with error bars indicating the standard deviation.

Data availability

The datasets generated during and/or analysed during the current study are available from the corresponding author on reasonable request. The SI videos can be found at this <https://doi.org/10.6084/m9.figshare.19608918.v1>.

Received: 4 March 2022; Accepted: 23 August 2022;

Published online: 06 September 2022

References

- Mewis, J. & Wagner, N. J. *Colloidal suspension rheology* (Cambridge University Press, 2012).
- Stickel, J. J. & Powell, R. L. Fluid mechanics and rheology of dense suspensions. *Annu. Rev. Fluid Mechanics*. **37**, 129–149 (2005).
- Osswald, T. & Rudolph, N. *Polymer rheology*. Carl Hanser, München (2015).
- David, N. V., Gao, X.-L. & Zheng, J. Q. Ballistic Resistant Body Armor: Contemporary and Prospective Materials and Related Protection Mechanisms. *Appl. Mechanics Rev.* **62** 050802(2009).
- Rus, D. & Tolley, M. T. Design, fabrication and control of soft robots. *Nature* **521**, 467–475 (2015).
- Josserand, C. & Thoroddsen, S. T. Drop impact on a solid surface. *Annu. Rev. Fluid Mechanics*. **48**, 365–391 (2016).
- Philippi, J., Lagrée, P.-Y. & Antkowiak, A. Drop impact on a solid surface: short-time self-similarity. *J. Fluid Mechanics*. **795**, 96–135 (2016).
- Laan, N., de Bruin, K. G., Bartolo, D., Josserand, C. & Bonn, D. Maximum diameter of impacting liquid droplets. *Phys. Rev. Appl.* **2**, 044018 (2014).
- Lee, J. B. et al. Universal rescaling of drop impact on smooth and rough surfaces. *J. Fluid Mechanics*. **786**, R4 (2016).
- Gordillo, L., Sun, T.-P. & Cheng, X. Dynamics of drop impact on solid surfaces: evolution of impact force and self-similar spreading. *J. Fluid Mechanics*. **840**, 190–214 (2018).
- Cheng, X., Sun, T.-P. & Gordillo, L. Drop impact dynamics: Impact force and stress distributions. *Annu. Rev. Fluid Mechanics*. **54**, 57–81 (2022).
- Bergeron, V., Bonn, D., Martin, J. Y. & Vovelle, L. Controlling droplet deposition with polymer additives. *Nature* **405**, 772–775 (2000).
- Blackwell, B. C., Deetjen, M. E., Gaudio, J. E. & Ewoldt, R. H. Sticking and splashing in yield-stress fluid drop impacts on coated surfaces. *Phys. Fluids*. **27**, 043101 (2015).
- Peters, I. R., Xu, Q. & Jaeger, H. M. Splashing onset in dense suspension droplets. *Phys. Rev. Lett.* **111**, 028301 (2013).
- Thoraval, M.-J. et al. Nanoscopic interactions of colloidal particles can suppress millimetre drop splashing. *Soft Matter*. **17**, 5116–5121 (2021).
- Boyer, F., Sandoval-Nava, E., Snoeijer, J. H., Dijkstra, J. F. & Lohse, D. Drop impact of shear thickening liquids. *Phys. Rev. Fluids*. **1**, 013901 (2016).
- Jørgensen, L., Forterre, Y. & Lhuissier, H. Deformation upon impact of a concentrated suspension drop. *J. Fluid Mechanics*. 896 (2020). <https://www.cambridge.org/core/services/aop-cambridge-core/content/view/C05D1B4CDE53506DC85FD69E7A03397C/S0022112020003948a.pdf/deformation-upon-impact-of-a-concentrated-suspension-drop.pdf>
- Bertola, V. & Haw, M. D. Impact of concentrated colloidal suspension drops on solid surfaces. *Powder Technol.* **270**, 412–417 (2015).
- Kim, G., Kim, W., Lee, S. & Jeon, S. Impact dynamics of a polystyrene suspension droplet on nonwetting surfaces measured using a quartz crystal microresonator and a high-speed camera. *Sensors Actuators B: Chem.* **288**, 716–720 (2019).
- Brown, E. & Jaeger, H. M. Shear thickening in concentrated suspensions: phenomenology, mechanisms and relations to jamming. *Reports Progress Phys.* **77**, 046602 (2014).
- Denn, M. M., Morris, J. F. & Bonn, D. Shear thickening in concentrated suspensions of smooth spheres in newtonian suspending fluids. *Soft Matter*. **14**, 170–184 (2018).
- Morris, J. F. Shear thickening of concentrated suspensions: Recent developments and relation to other phenomena. *Annu. Rev. Fluid Mechanics*. **52**, 121–144 (2020).
- Stöber, W., Fink, A. & Bohn, E. Controlled growth of monodisperse silica spheres in the micron size range. *J. Colloid Interface Sci.* **26**, 62–69 (1968).
- Zhang, L. et al. Hollow silica spheres: synthesis and mechanical properties. *Langmuir* **25**, 2711–2717 (2009).
- Whitmer, J. K. & Luijten, E. Sedimentation of aggregating colloids. *J. Chem. Phys.* **134**, 034510 (2011).
- Shajahan, T. & Breugem, W.-P. Influence of concentration on sedimentation of a dense suspension in a viscous fluid. *Flow, Turbulence Combustion*. **105**, 537–554 (2020).
- Supplementary Material, https://figshare.com/articles/media/Colloidal_drop_impact_SI_videos/19608918.
- Bi, D., Zhang, J., Chakraborty, B. & Behringer, R. P. Jamming by shear. *Nature* **480**, 355–358 (2011).
- James, N. M., Xue, H., Goyal, M. & Jaeger, H. M. Controlling shear jamming in dense suspensions via the particle aspect ratio. *Soft matter* **15**, 3649–3654 (2019).
- Scheller, B. L. & Bousfield, D. W. Newtonian drop impact with a solid surface. *AIChE J.* **41**, 1357–1367 (1995).
- Lagubeau, G. et al. Spreading dynamics of drop impacts. *J. Fluid Mechanics*. **713**, 50–60 (2012).
- Mitchell, B. R., Klewicki, J. C., Korkolis, Y. P. & Kinsey, B. L. The transient force profile of low-speed droplet impact: measurements and model. *J. Fluid Mechanics*. **867**, 300–322 (2019).
- Landau, L. D., Lifshitz, E. M., Kosevich, A. M. & Pitaevskii, L. P. Theory of elasticity: volume 7, vol. 7 (Elsevier, 1986).
- Rathee, V., Blair, D. L. & Urbach, J. S. Localized stress fluctuations drive shear thickening in dense suspensions. *Proceedings of the National Academy of Sciences of the United States of America* **114**, 8740–8745 (2017).
- Rathee, V., Blair, D. L. & Urbach, J. S. Localized transient jamming in discontinuous shear thickening. *J. Rheol.* **64**, 299–308 (2020).
- Rathee, V., Miller, J. M., Blair, D. L. & Urbach, J. S. Structure of propagating high stress fronts in a shear thickening suspension. *arXiv preprint arXiv:2203.02482* (2022).
- Han, E., Peters, I. R. & Jaeger, H. M. High-speed ultrasound imaging in dense suspensions reveals impact-activated solidification due to dynamic shear jamming. *Nat. commun.* **7**, 1–8 (2016).
- Waitukaitis, S. R. & Jaeger, H. M. Impact-activated solidification of dense suspensions via dynamic jamming fronts. *Nature* **487**, 205–209 (2012).
- Peters, I. R., Majumdar, S. & Jaeger, H. M. Direct observation of dynamic shear jamming in dense suspensions. *Nature* **532**, 214–217 (2016).
- Han, E., Wyart, M., Peters, I. R. & Jaeger, H. M. Shear fronts in shear-thickening suspensions. *Phys. Rev. Fluids*. **3**, 073301 (2018).
- Römcke, O., Peters, I. R. & Hearst, R. J. Getting jammed in all directions: Dynamic shear jamming around a cylinder towed through a dense suspension. *Phys. Rev. Fluids*. **6**, 063301 (2021).
- Liu, A. J. & Nagel, S. R. The jamming transition and the marginally jammed solid. *Annu. Rev. Conde. Matter Phys.* **1**, 347–369 (2010).
- Richard, D., Clanet, C. & Quéré, D. Contact time of a bouncing drop. *Nature* **417**, 811–811 (2002).

Acknowledgements

We thank Jeff Richards, Sid Nagel, and Xiang Cheng for useful discussions. This work was supported by the National Science Foundation under award number DMR-2004176. This work made use of the EPIC facility of Northwestern University's NUANCE Center, which has received support from the SHyNE Resource (NSF ECCS-2025633), the IIN, and Northwestern's MRSEC program (NSF DMR-1720139). We thank the Richards Lab at Northwestern University for the use of their rheometry facilities.

Author contributions

S.A. contributed to the conception of the work, experimental design, and data acquisition and analysis. P.S. contributed to data interpretation and analysis and drafted the manuscript. M.M.D. contributed to the conception of the work, data analysis and interpretation, and drafted the manuscript.

Competing interests

The authors declare no competing interests.

Additional information

Supplementary information The online version contains supplementary material available at <https://doi.org/10.1038/s42005-022-00998-w>.

Correspondence and requests for materials should be addressed to Michelle M. Driscoll.

Peer review information *Communications Physics* thanks Leonardo Gordillo and the other, anonymous, reviewer(s) for their contribution to the peer review of this work. Peer reviewer reports are available.

Reprints and permission information is available at <http://www.nature.com/reprints>

Publisher's note Springer Nature remains neutral with regard to jurisdictional claims in published maps and institutional affiliations.



Open Access This article is licensed under a Creative Commons Attribution 4.0 International License, which permits use, sharing, adaptation, distribution and reproduction in any medium or format, as long as you give appropriate credit to the original author(s) and the source, provide a link to the Creative Commons license, and indicate if changes were made. The images or other third party material in this article are included in the article's Creative Commons license, unless indicated otherwise in a credit line to the material. If material is not included in the article's Creative Commons license and your intended use is not permitted by statutory regulation or exceeds the permitted use, you will need to obtain permission directly from the copyright holder. To view a copy of this license, visit <http://creativecommons.org/licenses/by/4.0/>.

© The Author(s) 2022